Applied Catalysis B: Environmental 129 (2013) 501–508

Contents lists available at SciVerse ScienceDirect

Applied Catalysis B: Environmental

journal homepage: www.elsevier.com/locate/apcatb

Modelling of the kinetics of the catalytic soot oxidation on Fe_2O_3

Steffen Wagloehner, Sven Kureti*

Technical University of Freiberg, Department of Energy Process Engineering and Chemical Engineering, Fuchsmühlenweg 9, D-09596 Freiberg, Germany

ARTICLE INFO

Article history:
Received 3 June 2012
Received in revised form
24 September 2012
Accepted 29 September 2012
Available online 8 October 2012

Keywords:
Kinetic modelling
Soot oxidation
Fe_2O_3
Model catalyst
Fluid dynamics

ABSTRACT

This paper addresses the kinetic modelling of the soot oxidation on a Fe_2O_3 model catalyst. The kinetics was evaluated by temperature programmed oxidation using a packed bed of tight contact mixtures of Fe_2O_3 and soot. The reaction rate was expressed by a global-kinetic approach taken from a previous paper. Some kinetic parameters were determined by a fit to experimental TPO data using a stationary 1-D CSTR model with coupled mass and heat balance. The fitting led to an apparent activation energy of 73 kJ/mol, while the pre-exponential factor was calculated to be 1.6×10^3 $m^3/(mol\,s)$. The kinetic model was validated by simulations and was then implemented into a transient 2-D model of the fixed-bed reactor. This model implied the conservation of mass, heat and momentum and was checked by temperature measurements conducted with an IR camera. Finally, the 2-D model was validated by simulating some TPO investigations. The simulations provide local concentrations of CO_2, O_2 and soot as well as local temperature and gas velocity. Particularly, these results suggest the absence of any drastic gradients of concentration and temperature in the packed bed due to the convection of the gas stream.

1. Introduction

Diesel particulate filters (DPF) represent a common technology for the separation of soot from diesel exhaust. However, these filter systems need to be regenerated, as the trapped soot can cause backpressure effects potentially decreasing the engine efficiency [1]. Thus, several techniques were developed for the DPF regeneration, which imply the oxidation of the carbonaceous soot fraction, whereas ash entities remain in the filter. These procedures recently summarised in this journal [2] are (i) the Continuously Regenerating Trap (CRT) [3], which uses NO_2 for the initiation of the soot/O_2 reaction, (ii) organometallic Fuel Borne Catalysts decreasing the soot output of the engine and enhancing the oxidation of the filtered soot [4], and (iii) the post-injection of fuel causing rise in temperature [4,5]. Furthermore, the catalytic soot oxidation by O_2 is considered to be a promising alternative including a catalytic coating on the DPF (CDPF). A multitude of oxide catalysts was reported in the literature to enhance the soot/O_2 reaction, e.g. V_2O_5 [6], CeO_2 [7,8] and Fe_2O_3 [9]. But, up to now the CDPF technique reveals only limited benefit under real exhaust conditions due to insufficient contact of the catalytic coating and the soot deposited on it [10].

Mechanistic investigations showed that the role of the catalyst is to transfer oxygen from its surface to the soot [11]. Three basic oxygen transfer mechanisms are known for oxide catalysts [11–13]. (1) In the surface redox mechanism, e.g. reported for Co_3O_4, surface oxygen of the catalyst is transferred at the interface to the soot, whereas the resulting vacancies of the catalytic surface are filled by gas-phase oxygen. (2) The spill-over mechanism occurring on CeO_2 and Cr_2O_3 for instance implies dissociative adsorption of oxygen on the catalyst surface followed by transfer of atomic oxygen to the soot [12]. In this route, a contact of both solids is not explicitly required. (3) The redox mechanism reveals transfer of bulk oxygen from the catalyst to the contact points of both solids under local reduction of the catalyst; a prominent example is V_2O_5 [12]. The catalyst is then re-oxidised by gas-phase oxygen. In respect of Fe_2O_3, both surface [12,14,15] as well as bulk redox mechanism [2] was postulated in the literature. Additionally, another mechanism described for K/CeO_2 involves the formation of super oxides [16].

Moreover, catalysts were also classified into mobile and non-mobile systems. Mobile catalysts are alkaline, earth alkaline and several transition metals with low melting points [11,17,18]. These catalysts are capable of migrating onto the soot surface thus continuously forming new contact points. Contrary, non-mobile catalysts are temperature resistant oxides such as CeO_2 [7] and Fe_2O_3 [7,9,18], which essentially require contact to the soot. The effect of the type of contact on the soot oxidation was demonstrated by several groups indicating that intimate mixing of both solids enhances the soot oxidation [19,20]. Also, it was shown that soot oxidation can be strongly affected by the amount and heat capacity of the catalyst acting as a temperature buffer [2,21]. Furthermore, a global reaction mechanism of soot oxidation on Fe_2O_3 was reported implying the transfer of surface and crystal oxygen to the soot, the regeneration of oxygen vacancies and exchange of surface oxygen by CO_2 and O_2 adsorption [2,9,13].

* Corresponding author. Tel.: +49 3731 39 4482; fax: +49 3731 39 4555.
E-mail address: kureti@iec.tu-freiberg.de (S. Kureti).

0926-3373/$ – see front matter © 2012 Elsevier B.V. All rights reserved.
http://dx.doi.org/10.1016/j.apcatb.2012.09.055

For the use of iron oxide catalysts in the CDPF technique the present paper aims to contribute to a fundamental understanding of the oxidation of soot employing an α-Fe_2O_3 model catalyst. We report on kinetic investigations as well as a global-kinetic model, which we stepwise implemented into a stationary 1-D model and then a transient 2-D model.

2. Experimental

2.1. Preparation and characterisation of the Fe_2O_3 catalyst and soot

The α-Fe_2O_3 model catalyst was synthesised by polyvinyl alcohol (PVA) method as described in detail elsewhere [22]. Briefly, the remaining residual of the evaporated solution of aqueous $Fe(NO_3)_3$ and PVA was calcined in static air atmosphere at 600 °C for 5 h. The crystalline structure was analysed by powder X-ray diffraction (PXRD) on a D8 Advance (Bruker) using Ni filtered Cu Kα radiation. The BET surface area was examined by multi-point Sorptomatic 1990 (Porotec) taking N_2 as adsorbate. Before recording the isotherm at −196 °C, the sample was pre-treated at 300 °C for 2 h in vacuum (10^{-4} mbar). From the adsorption data taken at p/p_0 ratios between 0.05 and 0.30 the BET surface area was derived. The BET surface area of the catalyst was determined to be 15 m^2/g.

The soot was prepared by burning a C_3H_6/O_2 mixture in a diffusion flame and was collected by a particulate filter [23]. The most important physical–chemical properties of the soot are as follows: BET surface area: 90 m^2/g, amount of adsorbed species: 4 wt.%, chemical composition (adsorbed species neglected): 97.5 wt.% C, 1.5 wt.% O, 0.6 wt.% H, 0.2 wt.% N, soot is ashless, mean diameter of primary particles: 45 nm.

2.2. Kinetic studies

The kinetics of the soot oxidation on the α-Fe_2O_3 model catalyst was investigated by using the temperature programmed oxidation (TPO). In TPO, the temperature was linearly increased from room temperature to 500 °C at a rate of 3.3 K/min. The total gas flow was kept at 500 ml/min(STP) and consisted of 10 vol.% O_2 and 90 vol.% N_2 both supplied by independent flow controllers (MKS Instruments). Effluenting CO and CO_2 were analysed by a non-dispersive infrared spectrometer (Binos 1.2, Leybold-Heraeus). The experiments were performed with a tight contact catalyst/soot mixture implying 10 mmol catalyst and 5 mmol soot (m_{total} = 1.66 g). Tight contact mixture was established by ball milling the catalyst/soot blend for 15 min employing a Pulverisette 0 (Fritsch) with a hardened steel ball (m = 940 g); ball milling results in a contact mode being close to soot deposited on a catalytic DPF under full load conditions of the engine. After mixing, the respective mixture was pressed for 2 min at 4 MPa, granulated and sieved to a mesh of 125–250 μm to avoid discharge in the catalytic tests. Former investigations demonstrated that pressing and granulating do not affect the activity of the mixture, whereas the ball milling was found to be the crucial step of preparation [22]. Finally, the catalyst/soot mixture was placed in the quartz glass tube reactor (i.d. 10 mm) as packed bed fixed by quartz wool. The gas temperature was monitored by two K-type thermocouples located directly in front of and behind the bed.

The development of the local temperature of the tight contact catalyst/soot mixture was investigated by using an IR camera. A TPO was performed in a special stainless steel reactor (i.d. 10 mm) implying a sapphire window located above the packed bed. The temperature of the surface of the catalyst/soot bed was recorded by a Pyroview 380M camera (DIAS). The heating rate was 8.6 K/min.

3. Results and discussion

3.1. Modelling of the chemical kinetics

3.1.1. Development of a 1-D reactor model

For the development of a 1-D model a suitable reactor model was evaluated by determining the Bodenstein (Bo) number of the packed bed. We used an approach from Aris, which states the additivity of means and variances of the mean residence time distribution [24]. The mean residence time $\bar{t}$ and the variance σ^2 of the tube reactor ($\bar{t}$ = 37.8 s, σ^2 = 68.2 s^2), which includes the packed bed, and the empty tube reactor ($\bar{t}$ = 36.3 s with σ^2 = 40.9 s^2), shortened by the length of the packed bed, were determined by step experiments [25]. This facilitates the identification of the Bo number of the packed bed Eq. (1) resulting in Bo = 0.4 characterising a CSTR.

$$\frac{\sigma_2^2 - \sigma_1^2}{(\bar{t}_2 - \bar{t}_1)} = \frac{\Delta\sigma^2}{(\Delta\bar{t})^2} = \frac{1}{2 \cdot Bo} \tag{1}$$

Additionally, the Bo number of the packed bed was also estimated from the axial Peclet number ($Pe_{a,p}$) according to the equation of Edwards and Richardson, i.e. $1/Pe_{a,p} = 0.3/(Sc\,Re_p) + 0.5/(1 + 3.8/(Re_p\,Sc))$; Re_p is the particle Reynolds number and Sc is the Schmidt number [26]. With $Bo = Pe_{a,p}\,L/d_p$ (L, length of packed bed, d_p particle diameter) Bo is estimated to be 2 being close to the experimental result. Furthermore, packed beds with Bo numbers below 1 were also reported in the literature for similar conditions [27]. Nevertheless, it should be mentioned that the experimental Bo number is based on several simplifications. The retention time was measured at room temperature and possible changes in the packed bed due to conversion of soot upon TPO are not considered.

3.1.2. Coupling of kinetics and CSTR model

The rate of the CO_2 formation (Eq. (2)) is described by a global-kinetic expression depending on the concentration of gaseous O_2 ($c(O_2)$) and the molar amount of active carbon sites ($n(C^*)$) [14]. The rate constant k_{CO_2} is expressed by an Arrhenius-based approach. $n(C^*)$ is derived from a random pore model [9] which implies the surface concentration of active sites (λ), soot conversion (X), initial BET surface area (S_0), soot mass at conversion X ($m(X)$) and semi-empiric structural factor of soot (f) addressing the pore structure resulting in Eq. (3) [11].

$$r(CO_2) = \frac{dn(CO_2)}{dt} = k_{CO_2} \cdot n(C^*) \cdot c(O_2)^n \tag{2}$$

$$r(CO_2) = A \cdot \exp\left(\frac{-E}{RT}\right) \cdot m_0 \cdot (1 - X) \cdot S_0 \cdot \sqrt{1 + f \cdot X} \cdot c(O_2)^n \tag{3}$$

Moreover, the calculation of the Mears [28] and Weisz-Prater criteria [29] excludes mass transfer limitation by film and pore diffusion. However, it is known that the exothermic reaction and heat capacity of the packed bed [2] strongly affect the chemical kinetics of soot oxidation. Hence, Eq. (3) is coupled with the mass (Eq. (4); τ: hydrodynamic retention time, V_{bed}: bed volume) and energy balance (Eq. (5)) of the stationary CSTR; m is the reaction mass, $c_{p,bed}$ the heat capacity of the bed volume, $c_{p,gas}$ the heat capacity of the gas, ΔH the reaction heat, k the heat transfer coefficient and A is the heat transfer area.

$$\frac{dc(CO_2)}{dt} = \frac{1}{\tau}(c(CO_2)_{in} - c(CO_2)_{out}) + \frac{r(CO_2)}{V_{bed}} \tag{4}$$

$$m \cdot c_{p,bed} \cdot \frac{dT}{dt} = F \cdot c_{p,gas} \cdot (T_{furnace} - T) - r(CO_2) \cdot \Delta H - k \cdot A \cdot (T - T_{furnace}) \tag{5}$$

Table 1
Experimental data and parameters taken from literature for kinetic modelling.

Parameter	Value	Source
m_0	0.06 g	
S_0	90 m^2/g	[14]
f	60	[25]
λ	8.7×10^{-6} mol/m^2	[14]
$c(O_2)$	4.09 mol/m^3	
n	1	[11,40]
β	0.03 K/s	
V_{reac}	1.96×10^{-6} m^3	
F	8.3×10^{-6} m^3/s	
$c_{p,bed}$	145 J/(mol K)	[41]
$c_{p,gas}$	630 J/(m^3 K)	[25]
ΔH	−400 kJ/mol	[25]
A	7.85×10^{-4} m^2	
n_{cat}	5×10^{-3} mol	

The combination of these equations results in a system of two non-linear partial differential equations, which are solved by Malab tool ode113 (mass balance) and ode45 (energy balance) [30,31]. These differential equations are implemented in a self-developed program. The program calculates steady-state conditions for each temperature step by solving Eqs. (3)–(5) for $t \to \infty$. The amount of CO_2 formed in an interval from T_{n-1} to T_n, i.e. $\Delta n(CO_2)_T$, is determined from the heating rate β (Eq. (6)) and is used to calculate the soot conversion (Eq. (7)).

$$\Delta n(CO_2)_T = \frac{r(CO_2) \cdot (T_n - T_{n-1})}{\beta} \quad (6)$$

$$X(T) = \frac{\sum_{T=T_0}^{T} \Delta n(CO_2)_T}{n_{0,soot}} \quad (7)$$

Finally, the CO_2 fraction of the gas flow ($y(CO_2)$) corresponding to the molar CO_2 amount required for Eq. (2) is fitted to experimental data. For this purpose, a self-developed least-square estimator was taken using Excel software.

3.1.3. Determination of unknown parameters

For the reduction of the number of free parameters in the fitting procedure some parameters were taken from literature (Table 1). Furthermore, the volume of the packed bed implies a diameter of 0.01 m and a length of 0.025 m. Consequently, the remaining parameters to be determined are the pre-exponential factor A, the apparent activation energy E and the heat transfer coefficient k_0. The energy balance was experimentally checked by temperature measurements performed in the centre of the packed bed, i.e. at a length of ca. 0.0125 m corresponding to the outlet temperature of the CSTR model. The experimental basis of the fitting procedure was a TPO study performed with a heating rate of 1.8 K/min and an O_2 fraction of 10 vol.%; the remaining experimental parameters are demonstrated in Fig. 1.

Figs. 1 and 2 evidence that the calculated CO_2 fraction, soot conversion and temperature profile agree well with the experimental results. The maximum difference of modelled and measured temperatures is below 5 K, while CO_2 content and soot conversion only show certain divergence between 300 and 350 °C. The accuracy of the fitting procedure is also reflected by the high correlation coefficient (R^2) which is demonstrated in Table 2 along with the determined kinetic parameters. As referred to a previous study performed with same catalyst, soot and contact mode the apparent activation energy is found to be slightly smaller (73 kJ/mol vs. 78 kJ/mol). This difference is ascribed to the heat production of the soot oxidation considered in this paper by coupling the mass and heat balance (Eqs. (4) and (5)). As expected, the activation energy is clearly lower as compared to the non-catalytic oxidation of the soot taken (115 kJ/mol) [14]. A direct comparison with other literature data is difficult as the kinetic parameter are strongly related to the respective experimental conditions, e.g. mass of catalyst and soot, heating rate, contact mode and type of soot (Table 3). But, it can be summarised that the Fe_2O_3/soot mixture shows a relatively low apparent activation energy attributed to the reactivity of the soot as well as the effectiveness of the catalyst.

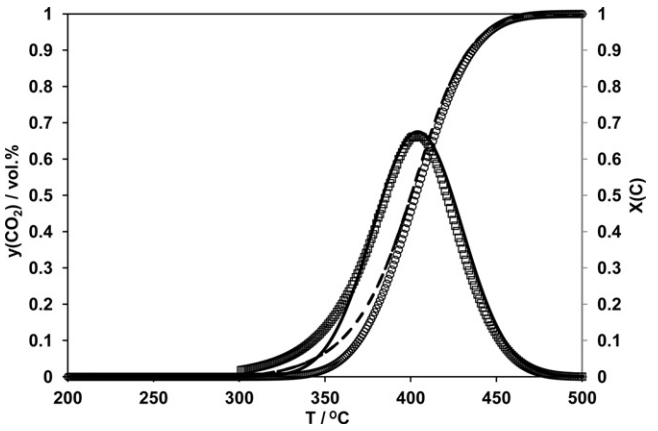

Fig. 1. CO_2 formation ((—) experimental, (□) calculated) as well as conversion of soot ((- - -) experimental, (σ) calculated) in the TPO of Fe_2O_3/soot. *Conditions*: F = 500 ml/min(STP), $y(O_2)$ = 10 vol.%, N_2 balance, β = 1.8 K/min, $n(Fe_2O_3)$ = 10 mmol, n(soot) = 5 mmol, tight contact mode.

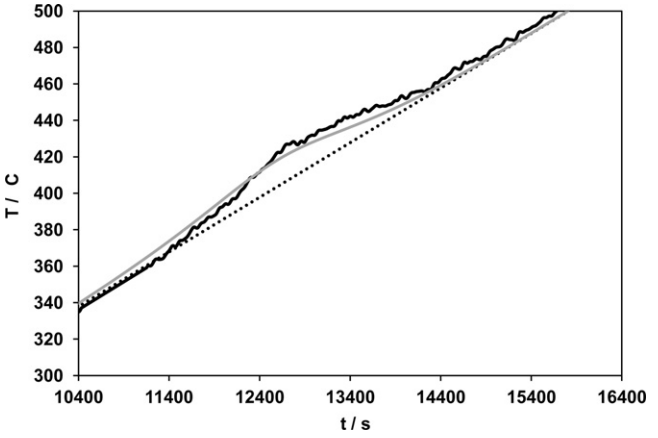

Fig. 2. Experimental ((···) gas inlet, (—) middle of packed bed) and modelled bed temperature ( ) in the TPO of Fe_2O_3/soot. *Conditions*: F = 500 ml/min(STP), $y(O_2)$ = 10 vol.%, N_2 balance, β = 1.8 K/min, $n(Fe_2O_3)$ = 10 mmol, n(soot) = 5 mmol, tight contact mode.

3.1.4. Validation of the kinetic model

For the validation of the kinetic model, TPO studies with varying heating rate and O_2 content were simulated by implementing the parameters demonstrated in Table 1 into the mass and energy balance of the CSTR model (Eqs. (4) and (5)). When the heating rate is varied the corresponding heat transfer coefficient k is derived from

Table 2
Kinetic parameters of the catalytic soot oxidation on Fe_2O_3 (R^2 = 0.986); calculation based on CSTR model. Reaction conditions are demonstrated in Fig. 1.

Parameter	Value
A	1.6×10^3 m^3/(mol s)
E	73 kJ/mol
k_0	121 W/(m^2 K)

Table 3
Activation energies of catalytic soot oxidation derived from literature.

System	Method	E (kJ/mol)	Source
C_3H_6-soot/Fe_2O_3, tight contact	Curve fit	78	[14]
Graphite/Fe_2O_3	Arrhenius plot	201	[42]
Diesel soot/CeO_2, loose contact	Redhead method [43]	159	[44]
Carbon black/CeO_2, tight contact	E-TEM	133	[45]
Carbon black/CeO_2, tight contact	Arrhenius plot [46]	65–90	[47]
Diesel soot/$Cs_4V_2O_7$, tight contact	Ozawa plot [48]	104	[49]
Diesel soot/K/CeO_2, tight contact	Arrhenius plot	74	[16]
Carbon black/K/Cu/Cl, tight contact	Arrhenius plot	85–100	[50]
Soot/Pt/Al_2O_3–CoO_x–PbO_x	Redhead method	101	[51]

k_0 and the ratio of β_0 and β (Eq. (8)); k_0 and β_0 refer to the heating ramp of 1.8 K/min.

$$k = \frac{k_0 \cdot \beta_0}{\beta} \tag{8}$$

Fig. 3 shows the simulation of a TPO with a heating ramp of 3.3 K/min, an O_2 content of 10 vol.% and a mixture of 2.5 mmol Fe_2O_3 and 5 mmol soot. The simulation predicts well the experimental traces, even the strong increase in CO_2 content. The difference in the simulated and experimental CO_2 fraction is <3% and the shift in temperature does not exceed 10 K.

Furthermore, when considering a O_2 content of 7.5 vol.%, a heating rate of 2 K/min and a blend of 10 mmol Fe_2O_3 and 5 mmol soot a good agreement of measured and predicted data is obtained as well (Fig. 4); the maximum CO_2 fraction exhibits a difference of 0.05 vol.%, while the temperature of maximum CO_2 content shows a deviation of 2 K only. These results exemplify the validity of the CSTR model implying the chemical kinetics.

3.2. Modelling of the fluid dynamics

To obtain further understanding of the catalytic soot oxidation the stationary 1-D CSTR model was extended to a transient 2-D model of the fixed-bed reactor including the conservation equations of mass and heat and momentum.

3.2.1. Setting-up of conservation equation

For the setting-up of the conservation equations the tube reactor was segmented into three control volumes, namely the area located in front of (area 1) and behind (area 3) the packed bed as well as the packed bed itself (area 2). To cover the transient experiments the mathematical expressions imply non-stationarity; for an optimum of quality and expenditure of time a two-dimensional

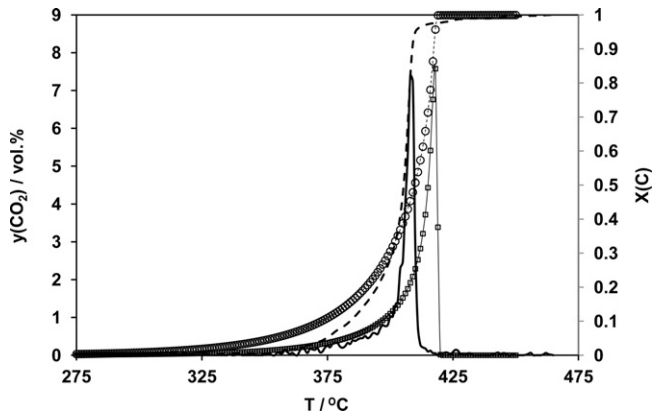

Fig. 3. CO_2 formation ((—) experimental, (□) simulated) as well as conversion of soot ((- - -) experimental, (σ) simulated) in the TPO of Fe_2O_3/soot. *Conditions*: F = 500 ml/min(STP), $y(O_2)$ = 10 vol.%, N_2 balance, β = 3.3 K/min, $n(Fe_2O_3)$ = 2.5 mmol, n(soot) = 5 mmol, tight contact mode.

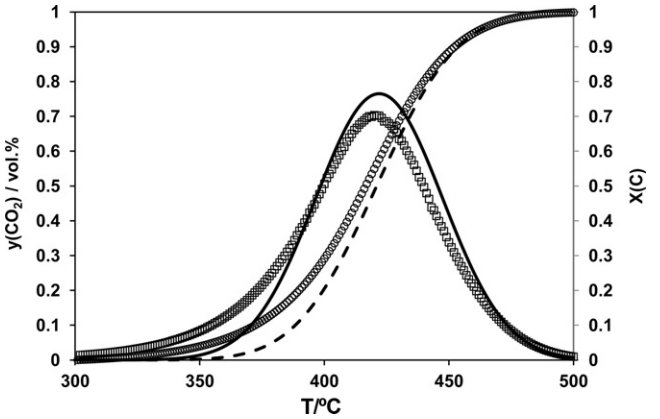

Fig. 4. CO_2 formation ((—) experimental, (□) simulated) as well as conversion of soot ((- - -) experimental, (○) simulated) in the TPO of Fe_2O_3/soot. *Conditions*: F = 500 ml/min(STP), $y(O_2)$ = 7.5 vol.%, N_2 balance, β = 2 K/min, $n(Fe_2O_3)$ = 10 mmol, n(soot) = 5 mmol, tight contact mode.

model was chosen. The transient heat transfer was described by convection and conduction, whereas an additional source term for heat production ($\dot{Q}$) was considered in the control volume of the packed bed (Eq. (9)); ρ is the density of air, c_p the heat capacity at constant pressure of air, k_{tc} the thermal conductivity and u is the velocity field supplied by the momentum transport. In areas 1 and 3 $\dot{Q}$ is zero, while in area 2 the heat source is calculated according to Eq. (10).

$$\rho c_{p,bed} \frac{\partial T}{\partial t} = \dot{Q} - \nabla(\rho c_p u T - k_{tc} \nabla T) \tag{9}$$

$$\dot{Q} = r(CO_2) \cdot (-\Delta H) \tag{10}$$

Heat capacity, density, thermal conductivity as well as dynamic viscosity are calculated for areas 1 and 3 in dependency of temperature; all values are provided by the Comsol properties database. For simplicity, the gas was assumed to be air. The specific parameters adapted to the above equations are summarised in Tables 4 and 5. The thermal conductivity in the packed bed (area 2) was determined by Eq. (11) assuming that the streamed porous medium is a continuum showing physical properties of the fluid and solid, whereas the soot is neglected due to its small mass fraction ($k_{Fe_2O_3}$:

Table 4
Properties of Fe_2O_3 and the packed bed.

Parameter	Denotation	Value
ε	Porosity of Fe_2O_3	0.509
κ	Permeability	2×10^{-11} m^2
d_{pore}	Pore diameter	1×10^{-5} m
k_{tc}	Thermal conductivity	0.14 W/(m K)
$k_{Fe_2O_3}$	Thermal conductivity Fe_2O_3	0.8365 W/(m K)
ε_{app}	Apparent porosity	0.2
τ	Tortuosity of Fe_2O_3	2
d_{p,Fe_2O_3}	Particle diameter of Fe_2O_3	70×10^{-6} m

Table 5
Initial values of the model (for tube reactor design).

Parameter	Denotation	Value
u	Velocity x-direction	0.074 m/s
v	Velocity y-direction	0 m/s
p	Pressure	1×10^5 Pa
$c(O_2)$	O_2 concentration	4.09 mol/m^3
$c(CO_2)$	CO_2 concentration	0 mol/m^3
$c(soot)$	Soot concentration	800 l/m^3

thermal conductivity of α-Fe_2O_3 [32], k_{gas}: thermal conductivity of air, ε_{app}: apparent porosity). This refers to the Brinkman equation widely used to describe the flow through porous media [33].

$$k_c = \varepsilon_{app} \cdot k_{Fe_2O_3} + (1 - \varepsilon_{app}) \cdot k_{gas} \quad (11)$$

The apparent porosity is determined by Eq. (12) to be 0.168 ($\rho_{Fe_2O_3}$: density of α-Fe_2O_3). Finally, k_c results in 0.18 W/(m K).

$$\varepsilon_{app} = \frac{m_{Fe_2O_3}/V_{bed}}{\rho_{Fe_2O_3}} \quad (12)$$

Mass transfer is expressed by convection and diffusion (areas 1 and 3), while the control volume of the packed bed additionally includes a term for the reaction (Eq. (13)); $c(i)$ is the concentration of species i and $D(i)_e$ the effective diffusion coefficient of O_2 and CO_2 in N_2. It should be mentioned here that in the fixed-bed the axial dispersion coefficient is not constant in length and therefore a specific term of diffusion is defined, while the remaining dispersion effects are considered by velocity field derived from the Brinkman equation (Eq. (14)).

$$\frac{\partial c(i)}{\partial t} = r(CO_2) - u \cdot \nabla c(i) - \nabla(-D(i)_e \nabla c(i)) \quad (13)$$

According to the Bosanquet equation $D(i)_e$ implies molecular diffusion in mesopores and macropores (D_{12}) and Knudsen diffusion in micropores (D_k) [34]. In the model, the binary diffusion of O_2 and CO_2 in N_2 was considered. D_{12} was calculated with the Fuller equation [35], while D_k was determined with the kinetic gas theory [36]. The tortuosity was assumed to be 2 [37].

The momentum transport in the control volumes of area 1 and area 2 exhibits pipe flow calculated with the Navier–Stokes equations [38]. For description of the momentum transport through the packed bed (area 2) the Brinkman equation was used (Eq. (14)) representing an extension of the Navier–Stokes equations and describing the flow in porous media when shear stresses in the fluid are of importance [24]. In Eq. (14), ρ is the density of air, η the dynamic viscosity of air, u the two-dimensional velocity field and I is the unit vector. The permeability κ depends on the properties of the fluid and the porous medium (Eq. (15)) [27].

$$\left(\frac{\rho}{\varepsilon}\right)\frac{\partial u}{\partial t} = \nabla \cdot \left[-pI + \left(\frac{1}{\varepsilon}\right)\left\{\eta(\nabla u + (\nabla u)^T) - \left(\frac{2\eta}{3}\right)(\nabla \cdot u)I\right\}\right] - \left(\frac{\eta}{\kappa}\right)u \quad (14)$$

$$\kappa = \frac{d_{pore}^2}{18}\left(3 + \frac{4}{1-\varepsilon} - 3\sqrt{\frac{8}{1-\varepsilon} - 3}\right) \quad (15)$$

In a first step the presented conservation equations were verified by comparing the temperature measurements performed by the IR camera in the special reactor with the surface temperature distribution calculated. Therefore, a formal kinetic expression for the reaction rate was simply used by fitting the corresponding CO_2 formation rate with a Gaussian expression (Origin 8.1 software). The analytical equation depends only on the temperature. The result of the Gaussian fit illustrates acceptable accordance with the experiment. Finally, the geometric dimensions of the reactor and the boundary conditions were formulated as shown in Fig. 5 as well as Tables 6 and 7. Then, the computation of the 2-D model was done by using the software COMSOL Multiphysics (version 3.5a). The comparison of the simulated and experimental results clearly shows that the model describes satisfactorily the TPO profile (Fig. 6). The production of CO_2 starts in the middle of the packed bed and the resulting increase in temperature is well reproduced by the simulation. But, due to the use of the Brinkman equation, the temperature distribution is more homogeneously as compared to the experiment. However, maximum differences between measured and simulated temperature are 20 K only confirming the reliability of the CFD model.

Table 6
Dimensions of the special reactor used for the IR camera measurements.

Boundary	Length (m)
$\omega1$, $\omega12$	3×10^{-3}
$\omega2$, $\omega3$, $\omega10$, $\omega11$	3×10^{-2}
$\omega6$, $\omega7$	2×10^{-2}
$\omega4$, $\omega5$, $\omega8$, $\omega9$	6×10^{-3}

Table 7
Boundary conditions for the conservation equations.

Boundary	Boundary condition
(a) Heat transport	
$\omega1$, $\omega12$	$n\cdot(-k\nabla T) = 0$
$\omega2$, $\omega3$, $\omega4$, $\omega5$, $\omega6$, $\omega7$, $\omega8$, $\omega9$, $\omega10$, $\omega11$	$T = T_e$[a]
(b) Mass transport	
$\omega1$	$c_i = c_{i0}$
$\omega2$, $\omega3$, $\omega4$, $\omega5$, $\omega6$, $\omega7$, $\omega8$, $\omega9$, $\omega10$, $\omega11$	$n\cdot N = 0$, $N = -D\nabla c_i + c_i u$
$\omega12$	$n\cdot(-D\nabla c_i) = 0$
(c) Momentum transport	
$\omega1$	$u = -u_0 \cdot n$
$\omega2$, $\omega3$, $\omega4$, $\omega5$, $\omega6$, $\omega7$, $\omega8$, $\omega9$, $\omega10$, $\omega11$	$u = 0$
$\omega12$	$\eta(\nabla u + (\nabla u)^T)n = 0$, $p = p_0$

[a] $T_e = \beta t$.

3.3. Coupling of chemical kinetics and fluid dynamics

The 2-D CFD model was transferred to the standard reactor used to resolve local concentrations, temperature and flow velocity upon a typical TPO study. For this purpose, the expression of the chemical kinetics was implemented into the conservation of mass and heat in the packed bed (area 2), whereas the rate of soot oxidation was described based on concentration of soot (c_{soot}) according to Eq. (16).

$$\frac{\partial c_{soot}}{\partial t} = \frac{-r_{CO_2}}{V_{bed}} \quad (16)$$

Eq. (16) was added to the system of conservation equations demonstrated in the previous section. The dimensions and boundaries of the reactor are depicted in Fig. 7 and are listed in Tables 8 and 9. With all these model parameters a TPO was simulated referring to a mixture of 10 mmol Fe_2O_3 and 5 mmol soot (c_{soot} = 800 mol/m^3), an O_2 content of 10 vol.% and a heating rate of 1.8 K/min.

Fig. 8 shows the simulated and experimental TPO profile indicating that the CO_2 trace is well predicted by the simulation. For instance, the difference in the inlet temperature, which

Table 8
Dimensions of the simulated reactor geometry (Fig. 7).

Boundary	Length (m)
$\omega1$, $\omega8$	10×10^{-3}
$\omega2$, $\omega3$, $\omega4$, $\omega5$, $\omega6$, $\omega7$	2.5×10^{-2}

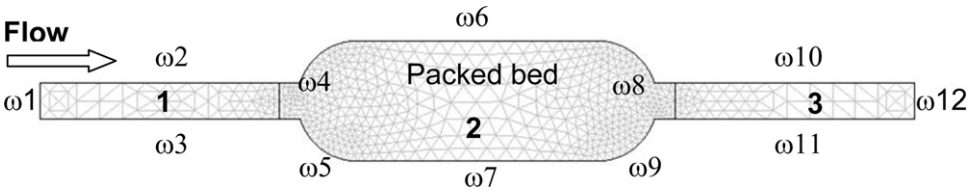

Fig. 5. Computational domains and boundaries of the 2-D model of the special reactor used for the IR camera measurements. The mesh consists of 1192 elements.

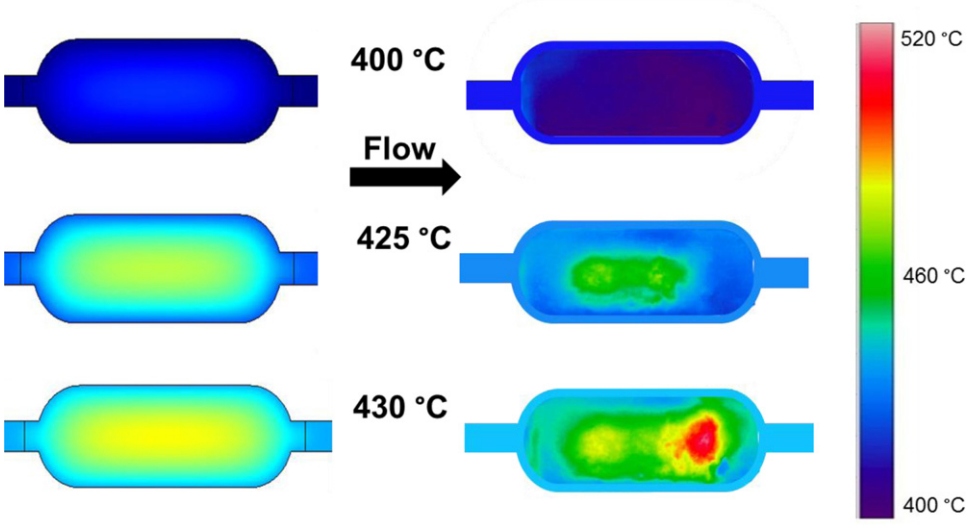

Fig. 6. Simulated (left) and experimental (right) surface temperature of the packed bed at three representative inlet temperatures upon a TPO of Fe_2O_3/soot performed in the special reactor for IR camera measurements. *Conditions*: F = 500 ml/min(STP), $y(O_2)$ = 10 vol.%, N_2 balance, β = 8.6 K/min, $n(Fe_2O_3)$ = 10 mmol, n(soot) = 5 mmol, tight contact mode.

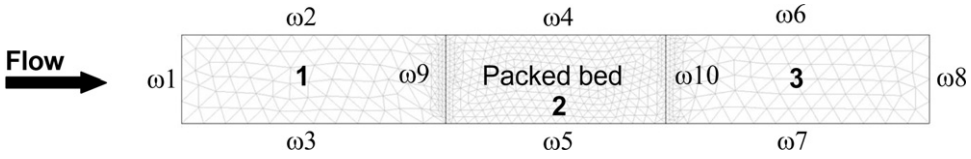

Fig. 7. Computational domains and boundaries of the 2-D model of the standard reactor. ω9 and ω10 are only valid for the equation of carbon oxidation. The mesh consists of 1129 elements.

Table 9
Boundary conditions for the conservation equations.

Boundary	Boundary condition
(a) Heat transport	
ω1, ω8	$n\cdot(-k\nabla T) = 0$
ω2, ω3, ω4, ω5, ω6, ω7, ω8	$T = T_e$[a]
(b) Mass transport	
ω1	$c_i = c_{i0}$
ω2, ω3, ω4, ω5, ω6, ω7	$n\cdot N = 0$, $N = -D\nabla c_i + c_i u$
ω8	$n\cdot(-D\nabla c_i) = 0$
(c) Momentum transport	
ω1	$u = -u_0\cdot n$
ω2, ω3, ω4, ω5, ω6, ω7	$u = 0$
ω8	$\eta(\nabla u + (\nabla u)^T)n = 0$, $p = p_0$
(d) Carbon combustion	
ω1, ω2, ω3, ω6, ω7, ω8	0
ω4, ω5, ω9, ω10	$n\cdot N = 0$, $N = -D\nabla c_{Carbon}$

[a] $T_e = \beta t$.

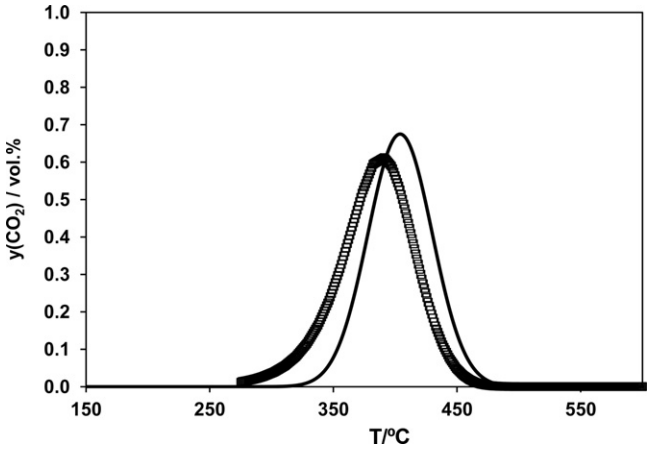

Fig. 8. Experimental (—) and calculated (□) CO_2 volume fractions in TPO of Fe_2O_3/soot performed in the standard reactor. Calculated CO_2 data refer to the last cell of the reactor outlet (r = 0, area 3). *Conditions*: F = 500 ml/min(STP), $y(O_2)$ = 10 vol.% O_2, N_2 balance, β = 1.8 K/min, (Fe_2O_3) = 10 mmol, n(soot) = 5 mmol, tight contact mode.

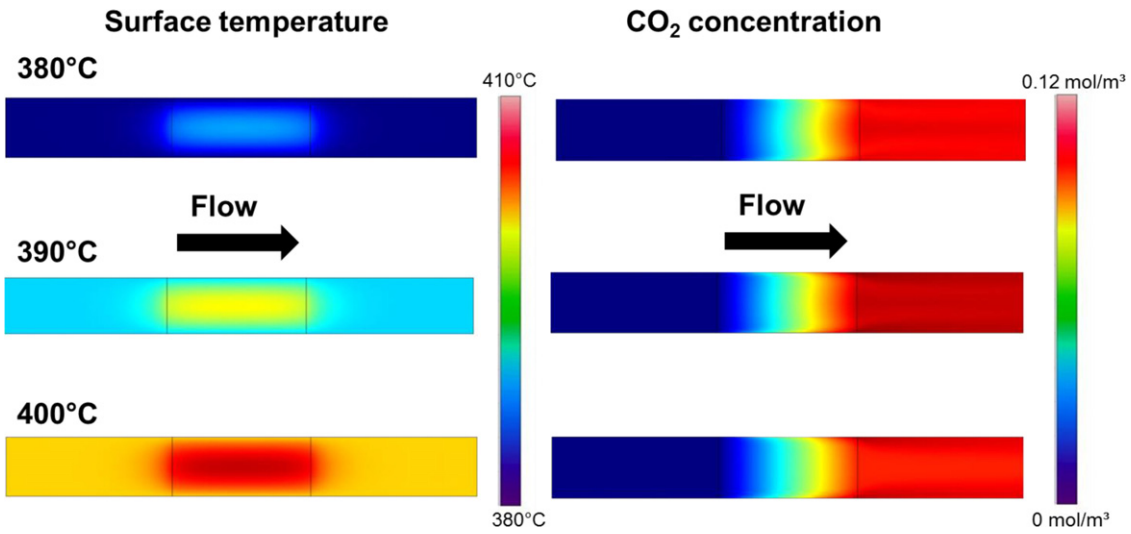

Fig. 9. Simulated surface temperature (left) and CO_2 concentration (right) of the packed bed at three representative inlet temperatures upon a TPO of Fe_2O_3/soot performed in the standard reactor. *Conditions*: F = 500 ml/min(STP), $y(O_2)$ = 5 vol.% O_2, N_2 balance, β = 1.8 K/min, $n(Fe_2O_3)$ = 10 mmol, n(soot) = 5 mmol, tight contact mode.

corresponds to the maximum CO_2 output fraction, is 11 K only being close the range of reproducibility of the TPO studies [25]. However, the predicted TPO data might also be a result of the kinetic parameters determined with a CSTR model implying lower efficiency as compared to a PFR. Thus, the kinetics described based on a CSTR model basically provide higher pre-exponential factor and lower activation energy. Furthermore, the simulated CO_2 concentration obtained in the last cell at the middle of the reactor outlet (area 3) coincides with the experimental value.

Furthermore, the simulation provides the local CO_2 concentration and surface temperature of the catalyst/soot mixture. Exemplarily, Fig. 9 shows three representative reactor inlet temperatures indicating simultaneous raise in CO_2 and temperature in the packed bed.

Moreover, CO_2 shows highest concentration behind the packed bed at the reactor wall (Fig. 9) being explained by the velocity field simulated. In areas 1 and 3 of the reactor the gas velocity reveals a non-disturbed laminar flow profile implying a laminar boundary layer near the reactor walls. Inside the bed the flow is influenced by the porous medium, which decreases the mean flow velocity. The resulting velocity distribution corresponds well with the CO_2 concentration exhibiting high content in proximity to the wall of the outlet part of the reactor (area 3). This increased proportion is interpreted with the slow discharge of CO_2 nearby the reactor wall; the flow is non-disturbed on the longitudinal axis of the tube reactor and thus it offers the highest velocity. Close to the wall the velocity is decreasing as a consequence of the friction (boundary condition u = 0 m/s). This effect goes along with a small convective part of the

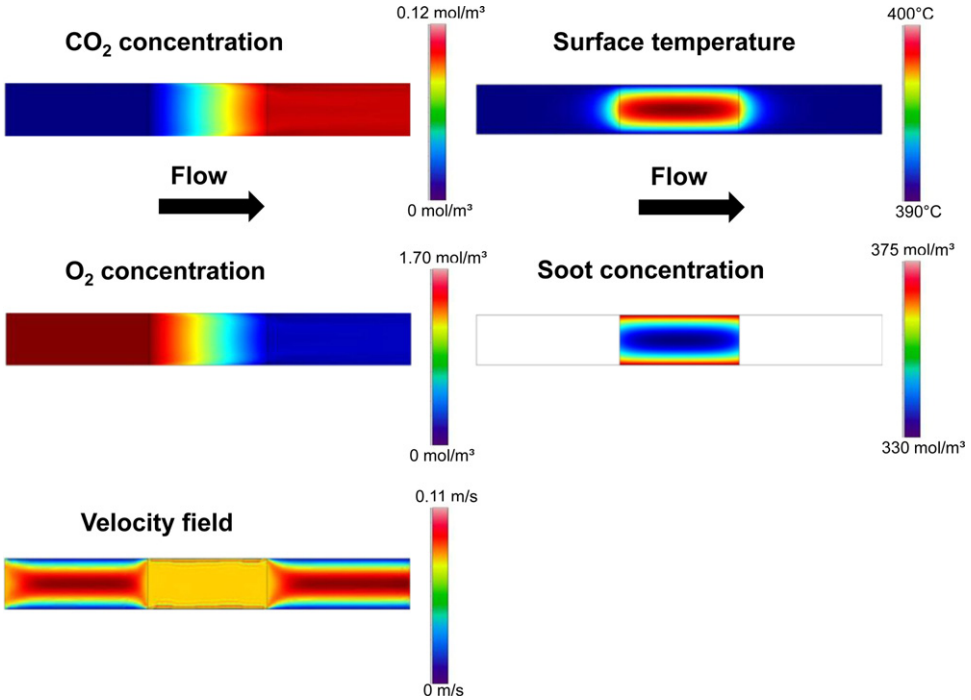

Fig. 10. Simulated CO_2 concentration, surface temperature, O_2 and carbon concentration as well as velocity field in TPO of Fe_2O_3/soot performed in the standard reactor at an inlet temperature of 390 °C. Conditions are demonstrated in Fig. 8.

mass transport resulting in the accumulation of CO_2 in the boundary layers. Furthermore, the temperature raise in the packed bed reveals an increase of 10 K being in the same range as the experimental temperature (Fig. 2). The soot conversion is initiated in the middle of the packed bed and proceeds to the walls of the reactor corresponding to the heat distribution in the packed bed. The high temperature in the middle of the packed bed may be attributed to the boundary current. The packed bed induces a high velocity on the boundaries of the bed and a low velocity in the middle (Fig. 10). This suggests low convectional heat extraction in the middle leading to accumulation of heat. Hence, the temperature in the middle exceeds that of the boundaries resulting in the initiation of the reaction from the middle of the packed bed (Fig. 9). The simulated O_2 concentration shows sufficient oxygen in the whole catalyst/soot bed, even at highest CO_2 fraction (1.7 mol/m^3 corresponding to ca. 9 vol.%). This indicates that the rate of soot oxidation is not limited by deficient supply of O_2.

4. Conclusion

The present study dealt with the coupling of the fluid dynamics and chemical kinetics of the soot oxidation on a Fe_2O_3 model catalyst. It was shown that the fixed bed of the catalyst and soot mixture could be described by a stationary CSTR model implying gradient-free concentrations and temperature. Then, a global-kinetic approach was implemented into this reactor model including the equations of mass and heat conservation. The relevance of the kinetic model was proven by simulations.

Finally, the kinetic model was transferred to a non-stationary 2-D model of the reactor providing detailed insights into the coupling of chemical kinetics and fluid dynamics. This coupled model predicted experimental data well. Furthermore, the transient behaviour of the reaction system and local proportion of soot, O_2 and CO_2 as well as temperature and flow gradients were simulated. The results of the simulations excluded any hot spots or significant concentrations gradients due to the catalytic soot oxidation. All gradients of concentrations and temperature were mainly driven by the fluid dynamics. Thus, the model provides insights into important parameters, which are experimentally hard to determine. To obtain further knowledge in future work the model may be extended to loose contact mixtures of catalyst and soot and both modes of contact blends should be implemented into a model of real DPF systems [39].

Acknowledgement

We thankfully acknowledge the cooperation and financial support of Umicore (Hanau).

References

[1] B.A.A.L. van Setten, M. Makkee, J.A. Moulijn, Catalysis Reviews 43 (2001) 489.
[2] S. Wagloehner, S. Kureti, Applied Catalysis B: Environmental 125 (2012) 158.
[3] A. Setiabudi, B.A.A.L. van Setten, M. Makkee, J.A. Moulijn, Applied Catalysis B: Environmental 35 (2002) 159.
[4] O. Salvat, P. Marez, G. Belot, SAE Technical Paper Series 2000-01-0473.
[5] P. Zelenka, W. Cartellieri, P. Duke, Applied Catalysis B: Environmental 7 (1996) 3.
[6] Y. Teraoka, K. Nakano, S. Kagawa, W.F. Shanguan, Applied Catalysis B: Environmental 5 (1995) 181.
[7] E. Aneggi, C.d. Leitenburg, G. Dolcetti, A. Trovarelli, Catalysis Today 114 (2006) 40.
[8] A. Bueno-López, K. Krishna, M. Makkee, J.A. Moulijn, Journal of Catalysis 230 (2005) 237.
[9] D. Reichert, H. Bockhorn, S. Kureti, Applied Catalysis B: Environmental 80 (2008) 248.
[10] B.W.L. Southward, S. Basso, SAE Technical Paper Series 1 (2009) 239.
[11] D. Reichert, Untersuchungen zur Reaktion von Stickstoffoxiden und Sauerstoff am Katalysator α-Fe_2O_3, Universität Karlsruhe (TH), Karlsruhe, 2008.
[12] G. Mul, F. Kapteijn, C. Doornkamp, J.A. Moulijn, Journal of Catalysis 179 (1998) 258.
[13] G. Mul, J.P.A. Neeft, F. Kapteijn, J.A. Moulijn, Carbon 36 (1997) 1269.
[14] D. Reichert, T. Finke, N. Atanassova, H. Bockhorn, S. Kureti, Applied Catalysis B: Environmental 84 (2008) 803.
[15] Z. Zhang, D. Han, S. Wei, Y. Zhang, Journal of Catalysis 276 (2010) 16.
[16] M.S. Gross, M.A. Ulla, C.A. Querini, Applied Catalysis A: General 360 (2009) 81.
[17] B.R. Stanmore, J.F. Brilhac, P. Gilot, Carbon 39 (2001) 2247.
[18] V. Serra, G. Saracco, C. Badini, V. Specchia, Applied Catalysis B: Environmental 11 (1997) 329.
[19] J.P.A. Neeft, O.P.v. Pruissen, M. Makkee, J.A. Moulijn, Applied Catalysis B: Environmental 12 (1997) 21.
[20] B.A.A.L. van Setten, J.M. Schouten, M. Makkee, J.A. Moulijn, Applied Catalysis B: Environmental 28 (2000) 253.
[21] J.P.A. Neeft, F. Hoornaert, M. Makkee, J.A. Moulijn, Thermochimica Acta 287 (1996) 261.
[22] S. Kureti, K. Hizbullah, W. Weisweiler, Applied Catalysis B: Environmental 3 (2003) 281.
[23] P. Balle, H. Bockhorn, B. Geiger, N. Jan, S. Kureti, D. Reichert, T. Schröder, Chemical Engineering and Processing 45 (2006) 1065.
[24] O. Levenspiel, Chemical Reaction Engineering, Jon Wiley & Sons, 1999.
[25] S. Wagloehner, Soot Oxidation on Iron Oxide Catalysts, Karlsruhe Institute of Technology, Karlsruhe, 2012.
[26] C.Y. Wen, L.T. Fan, Models for Flow Systems and Chemical Reactors, Marcel Dekker, New York, 1975.
[27] J.J. Carberry, R.H. Bretton, AIChE Journal 4 (1958) 367.
[28] D.E. Mears, Industrial and Engineering Chemistry Process Design and Development 10 (1971) 541.
[29] M. Baerns, H. Hofmann, A. Renken, Chemische Reaktionstechnik, Georg Thieme Verlag, Stuttgart, 1987.
[30] A. Angermann, M. Beuschel, M. Rau, U. Wohlfahrt, Matlab-Simulink-Stateflow, Oldenbourg-Verlag, München Wien, 2005.
[31] A. Biran, M. Breiner, Matlab 5 für Ingenieure, Addison-Wesley-Verlag, 1999.
[32] J. Koenigsberger, J. Weiss, Annalen der Physik 4 (1911).
[33] A.E. Scheidegger, The Physics of Flow Through Porous Media, University of Toronto, Toronto, 1973.
[34] C.H. Bosanquet, British TA Report BR-507, 1944.
[35] E.N. Fuller, P.D. Schettler, J.C. Giddings, Industrial and Engineering Chemistry 58 (1966) 18.
[36] A.E. Scheidegger, The Physics of Flow Through Porous Media, University of Toronto Press, 1974.
[37] J. vanBrakel, P.M. Heertjes, International Journal of Heat and Mass Transfer 17 (1974) 1093.
[38] G.K. Batchelor, An Introduction to Fluid Mechanics, Cambridge University Press, 2000.
[39] J.F. Knoth, A. Drochner, H. Vogel, J. Gieshoff, M. Kögel, M. Pfeiffer, M. Votsmeier, Catalysis Today 105 (2005) 598.
[40] J.P.A. Neeft, T.X. Nijhuis, E. Smakman, M. Makkee, J.A. Moulijn, Fuel 76 (1997) 1129.
[41] C.L. Snow, C.R. Lee, Q. Shi, J. Boerio-Goates, B.F. Woodfield, Journal of Chemical Thermodynamics 42 (2010) 1142.
[42] E.A. Heintz, W.E. Parker, Carbon 4 (1966) 473.
[43] P.A. Redhead, Vacuum 12 (1962) 203.
[44] B. Dernaika, D. Uner, Applied Catalysis B: Environmental 40 (2003) 219.
[45] S.B. Simonsen, S. Dahl, E. Johnson, S. Helveg, Journal of Catalysis 255 (2008) 1.
[46] P. Atkins, J.D. Paula, Atkins' Physical Chemistry, Oxford University Press, 2006.
[47] M.N. Bokova, C. Decarne, E. Abi-Aad, A.N. Pryakhin, V.V. Lunin, A. Aboukais, Thermochimica Acta 428 (2005) 165.
[48] T. Ozawa, Journal of Thermal Analysis and Calorimetry 2 (1970) 301.
[49] D. Fino, N. Russo, C. Badini, G. Saracco, V. Specchia, AIChE Journal 49 (2003) 2173.
[50] P. Ciambelli, P. Parrella, S. Vaccaro, Studies in Surface Science and Catalysis 71 (1991) 323.
[51] D. Uner, M.K. Demikrol, B. Dernaika, Applied Catalysis B: Environmental 61 (2005) 334.